PERGAMON

International Journal of Rock Mechanics & Mining Sciences 38 (2001) 765–776

International Journal of
Rock Mechanics
and Mining Sciences

www.elsevier.com/locate/ijrmms

Compressional waves guided between parallel fractures

Changjiu Xian[a], D.D. Nolte[b], L.J. Pyrak-Nolte[a,b,*]

[a] *Department of Earth and Atmospheric Sciences, Purdue University, West Lafayette, IN, USA*
[b] *Department of Physics, Purdue University, West Lafayette, IN, USA*

Accepted 17 July 2001

Abstract

We have performed experiments on the laboratory scale to image seismic wavefronts of compressional waves that are guided between parallel fractures. The wavefronts are detected using water-coupled 1 MHz piezoelectric transducers. The stiffness of the fractures is controlled by applying radial stress in a hydraulic stress apparatus that leaves the observation face of the fractured sample open to measurement. The two fractures form a waveguide in isotropic homogeneous aluminum and act as parallel displacement-discontinuity boundary conditions separated by a distance $d \approx 2\lambda$. The compressional wave is a leaky guided mode that sheds energy into the medium beyond the fractures. However, the fractures provide sufficiently strong energy confinement inside the central waveguide for a sample length L of approximately $L \approx 15\lambda$ to observe the guided wave. Fractures with low fracture specific stifffness produce strong energy confinement in the guided compressional-mode wave. © 2001 Published by Elsevier Science Ltd.

1. Introduction

Successful sequestration of nuclear waste, contaminants or other fluids in active or depleted oil or gas reservoirs, or man-made underground structures, requires an accurate map of the hydraulic and mechanical integrity of a site. Rock engineering in fractured rock masses requires that geophysical site characterization extract information on the location, number, and properties of fractures. Fractures are the principle source of hydraulic and mechanical anisotropy and heterogeneity in a rock mass. These discontinuities are planes of mechanical instability and often have effective permeabilities that far exceed the permeability of the rock matrix. Despite the importance of fractures, wave propagation through fractured rock has traditionally been modeled using effective medium theories [1–3] that use a static approximation to develop analytic expressions for the elastic moduli of a population of microcracks or multiple fracture sets [4–6]. This approach assumes that a fracture reduces the modulus of the rock and thus reduces the seismic velocity. The effect of the fracture is distributed throughout the bulk and the discreteness of the fracture is lost. Hence a reduction in velocity is observed, but the cause of the reduction cannot be located. In addition, for a purely elastic system, effective moduli theories predict frequency-independent seismic velocities. Advances in locating and characterizing fractures using seismic methods can be achieved through a better understanding of discrete effects of fractures that produce seismic anisotropy and a frequency-dependent seismic response of a fracture or sets of fractures.

The frequency-dependent seismic response of fractured rock can be attributed to two distinctly different mechanisms. First, fractures have an intrinsic frequency dependence caused by a discontinuity in strain when a seismic wave propagates along or across a fracture. This intrinsic frequency-dependent seismic response is easily simulated using the displacement discontinuity theory or non-welded contact theory [7–10]. The displacement discontinuity theory retains the discreteness of the fracture and although it is a purely elastic case, it results in frequency-dependent seismic velocities, as well as frequency-dependent transmission and reflection coefficients.

The second source of frequency-dependent seismic anisotropy in a fractured rock arises from sets of multiple fractures. The spacing between multiple parallel fractures introduces a characteristic length scale for the rock mass. A seismic wave will be increasingly scattered

*Corresponding author. Department of Physics, Purdue University, 1396 Physics Building, West Lafayette, IN 47907-1396, USA. Tel.: +1-765-494-3027; fax: +1-765-494-0706.

E-mail address: ljpn@physics.purdue.edu (L.J. Pyrak-Nolte).

1365-1609/01/$ - see front matter © 2001 Published by Elsevier Science Ltd.
PII: S1365-1609(01)00041-7

as the wavelength of the seismic signal approaches the characteristic length scale of the medium, in this case the fracture spacing. This characteristic length scale results in a frequency-dependent seismic response that manifests itself as scattering, resonance [11], and waveguiding [12]. For plane waves, this characteristic length scale results in a frequency-dependent seismic response that produces stop-band behavior when wave modes cease to propagate perpendicular to periodic sets of fractures for a band of frequencies that are related to the stiffness of the fracture and fracture spacing [11].

Our primary experimental goal in this paper is to image seismic waves propagating parallel to multiple fractures using a spatially localized source, i.e., a source that is localized within a single layer defined by two parallel fractures. We image the spatial and temporal distribution of energy in a sample containing multiple parallel fractures with a fracture spacing comparable to a wavelength. The resulting wavefronts show energy confinement between fractures that is a function of fracture specific stiffness.

2. Experimental set-up

To measure the seismic properties of the fracture waveguide, we use an acoustic wavefront imaging method [13–16]. This technique is capable of acquiring the full arriving waveform in two spatial dimensions and one temporal dimension. From this three-dimensional dataset, we reconstruct the complete longitudinal components of acoustic wavefronts that have propagated through a sample, and thereby obtain a direct visualization of discontinuous features in the arriving wavefronts produced by the presence of discrete fractures.

Two samples were used to study wave propagation parallel to sets of multiple parallel fractures. The samples were made from aluminum which is an isotropic, homogeneous material that has low attenuation. Any distortion to the propagating wavefront is caused by the fractures and not by the bulk material. The compressional wave velocity of aluminum is 6500 m/s and the shear wave velocity is 3300 m/s. Two cylindrical samples were used in this study, one an intact sample, FI, that contained no fractures, and sample F12 which contained seven ideal fractures with a fracture spacing of 12 mm. The fracture surfaces were polished. Both samples were 92 mm in diameter. Sample FI was 106 mm in length and sample F12 was 102 mm in length. In addition to sample F12, Xian [34] also performed the same experiments on samples containing fractures spaced 3, 6, and 25 mm apart.

Two sets of transducers were used in this study: (1) spherically focused transducers (1 MHz) were used for imaging the propagating wavefront; and (2) plane-wave transducers (1 MHz) were used to study the dispersion properties of compressional-mode guided waves between two parallel fractures. Wavelet analysis of a signal propagated through sample FI using the spherically focused transducers and the plane-wave transducers showed that the dominant frequency (i.e., the frequency at which most of the energy is propagating) is 0.5 and 1.0 MHz, respectively. Thus, for experiments using the spherically focused transducers, for sample F12, the ratio of signal wavelength to fracture spacing was $\lambda/d = 1.08$. For experiments using the plane-wave transducers, for sample F12, the ratio of signal wavelength to fracture spacing was $\lambda/d = 0.542$.

Prior to assembling a sample, the surfaces of the fractures and the ends of the samples are cleaned with a petroleum distillate to remove possible adhesives followed by acetone and methanol. The fracture samples are composed of a set of plates wrapped by cellophane tape around the circumference of the sample. For measurements made in the dry condition, a single layer of cellophane tape is placed on the ends of the sample to maintain dryness. Xian [34] also performed the same measurements for the saturated condition which are not presented in this paper.

The assembled sample is placed in a rubber-lined confining cell. The rubber prevents the oil, which is used to apply stress around the circumference of the sample, from penetrating the sample. In the confining cell (Fig. 1), the sample is oriented such that the fractures are vertical. Measurements were made on each sample for 0, 1.4, 4 and 7 MPa confining pressures. An electronic pressure transducer (Transmetric P27EG) was used to monitor the confining pressure throughout the duration of the experiment.

The acoustic wavefront imaging system (Fig. 2) is equipped with spherically focused water-coupled source and receiver transducers with central frequencies of 0.5 MHz which roughly corresponds to a signal wavelength of 13 mm in aluminum. In wavefront imaging, the source is maintained at a fixed location while the receiver is moved to record the data over a two-dimensional region to obtain the spatial distribution of energy with time (approximately 3600 waveforms per sample). Water-coupled transducers are used to provide

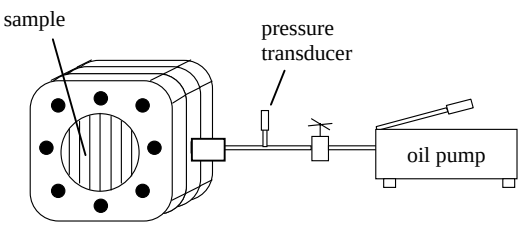

Fig. 1. Sketch of sample positioned in confining cell (maximum confining pressure = 10.3 MPa).

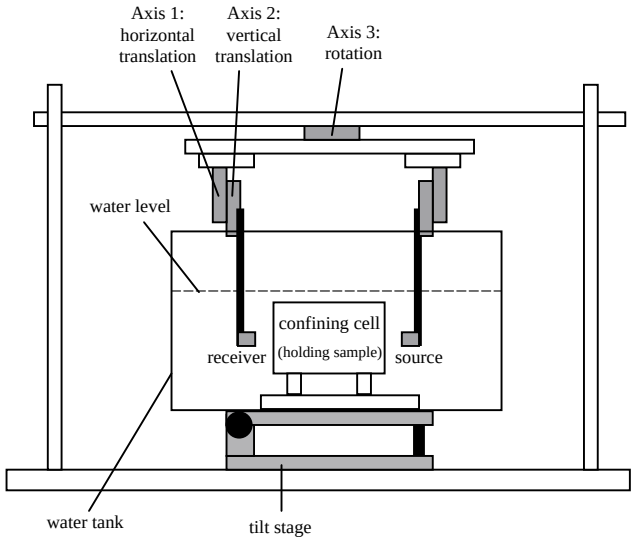

Fig. 2. Sketch of the acoustic wavefront imaging system. The confining cell (Fig. 1) is placed in the water tank. Water is the couplant between the source and receiving transducers. Axis 1 and 2 consist of computer controlled translation stages used to collect data in a two dimensional region (Fig. 3). Axis 3 and the tilt stage are used for alignment of the sample.

uniform coupling between the transducers and the sample for all locations on the sample. Spherically focused transducers generate a finite spot size which produces a pseudo-spherical wavefront for the source and which for the receiver results in a finite-size probe. The spot size (beam diameter) for the transducers used for this investigation is 2 mm (in water).

To perform a measurement, the confining cell is placed between the source and receiving transducers. The source and receiver are focused on the surface of the end of a sample (a focal distance of approximately 31.75 mm measured from the front edge of the transducer). Alignment of the source and receiving transducers relative to each other and the sample is important to ensure that the acoustic response observed for different samples is produced by variations in the sample and not variations in the set-up. Before placement of the confining cell into the wavefront imaging tank (Fig. 2), the faces of the source and receiving transducers are aligned parallel to each other. Alignment of the sample relative to the transducers is performed using the arrival time of the reflected wave from the end of the sample to ensure that the source and receiving transducers are parallel to the ends of the sample. A rotary stage and a tilt stage (Fig. 2) are used to align the sample relative to the transducers. The reflected wave arrival time is maintained to within $+0.025\,\mu s$ over the $60\,mm \times 60\,mm$ sampling region. Alignment of the sample is rechecked when pressure is applied to the sample.

For wavefront imaging, the source is held fixed and the receiver is moved in 1 mm increments over a $60\,mm \times 60\,mm$ area. The translation of the receiving transducer is performed using computer-controlled linear actuators (Newport 850-B4 with Newport Motion Master 2000). The input pulse to the transducers (for both the intact and fractured samples) consists of a 150 V square pulse (IRCO—M1k-20 pulse generator) with a $0.3\,\mu s$ duration and a repetition rate of 100 Hz. The received waveforms are amplified by 34 dB (Panametrics PR500). At each receiving location, 2000 points of the waveform are recorded, which represents a 20 microsecond window containing the compressional-wave and other arrivals. The received waveforms were digitized (Lecroy 9314L) and stored on a computer for analysis. The system delay for this experiment includes the time the wave travels through the water and any delays caused by the electronics of the system. The system delay is $46.89\,\mu s$ when using the spherically focused transducers.

Fig. 3 shows the source location for each sample. The source position was chosen to enable location of the source between fractures, i.e., within a layer. Five fractures were in the sample region for sample F12. For the intact sample, FI, measurements were made with the source shifted 5 mm from the center to be equivalent to the source location for the F12 sample.

The spherically focused transducers are appropriate for wavefront imaging. However, the theory for wave-guiding (see Section 4.2) is based on plane-wave propagation. Therefore, measurements of energy confinement by parallel fractures was also investigated using immersion plane-wave compressional-mode transducers. As described earlier in this section, the plane-wave transducers result in a dominant frequency of 1 MHz resulting in a wavelength of $\lambda = 6.5\,mm$. For sample F12, the fracture spacing is $d = 12\,mm$ which results in $d \sim 2\lambda$. The source and receiver plane wave transducers were placed 20 mm from the surface of the sample.

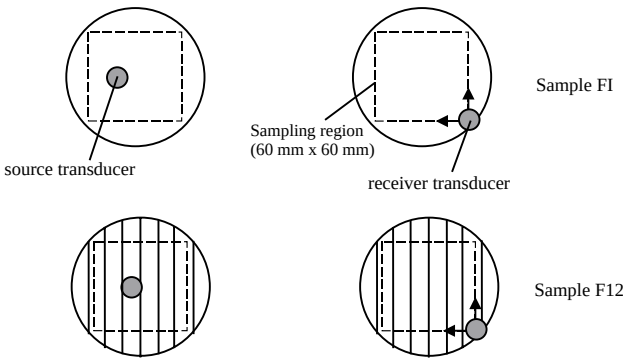

Fig. 3. Diagram of source location and receiver sampling region for sample FI and F12. For sample F12, only five fractures are probed in the sampling region.

3. Results

3.1. Individual waveforms

Thirty-six hundred received waveforms were collected for each sample to study the effect of multiple parallel fractures on a propagating acoustic wavefront. Figs. 4 and 5 show the received waveforms (collected using the spherically focused transducers) for samples FI and F12, respectively, for the case when the source and receiver are each positioned at the center of the layer. In Fig. 4, received waveforms for the solid sample, FI, are shown for 0 and 7 MPa confining pressures. Applying a confining pressure to the sample FI had no effect on the amplitude or arrival time of the waves. For sample F12 (Fig. 5), the energy confined to the layer decreased as the confining pressure was increased from 0 to 7 MPa, with a noticeably greater decrease in the energy of the later arriving energy (for times $>66\,\mu s$).

3.2. Wavefront as a function of time

Our wavefront imaging apparatus for data collection enables us to visualize the arriving wavefront as a function of time. Fig. 6 shows the arriving acoustic wavefront as a function of position and time for sample FI. The color in the images corresponds to the amplitude (in volts) of the signal. For example, the signal for sample FI subjected to 7 MPa (Fig. 4) corresponds to the signal in Fig. 6b at a position of 24 mm. The first positive peak of the waveform in Fig. 4 is represented by red in Fig. 6b and the following negative peak (or first trough) is represented by blue. The wavefronts that have been reflected from the circumference of the sample appear at a position of 43 mm.

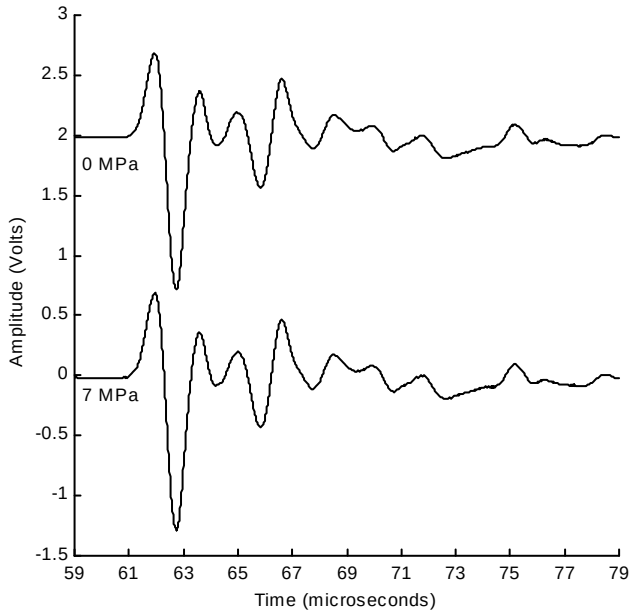

Fig. 4. The received waveforms from the intact sample FI subjected to 0 and 7 MPa when the source and receiver are positioned across from each other.

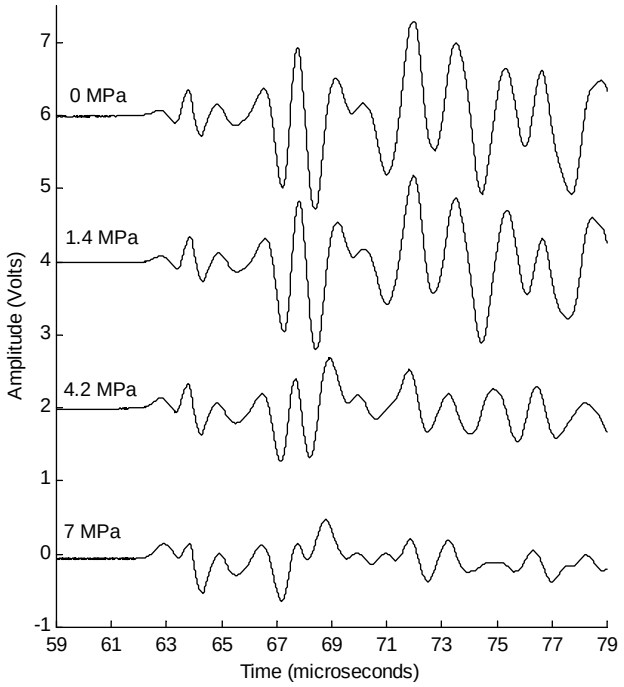

Fig. 5. The received waveforms from sample F12 subjected to 0, 1.4, 4.2 and 7 MPa when the source and receiver are positioned across from each other in a layer (Fig. 3).

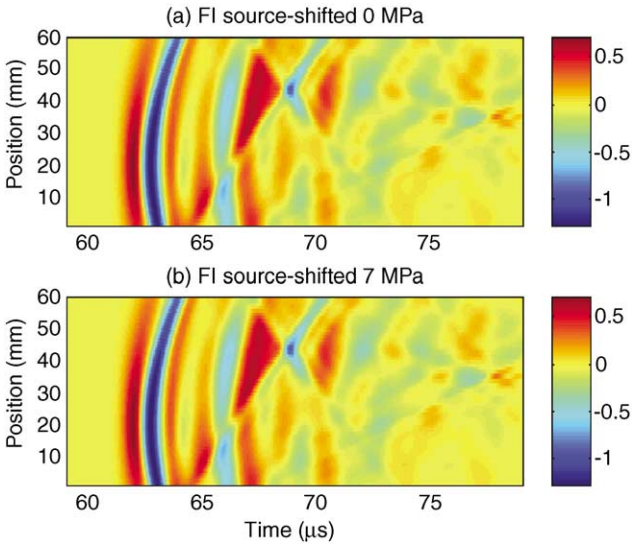

Fig. 6. The seismic wavefront as a function of position and time from the intact sample FI subjected to (a) 0 MPa and (b) 7 MPa. The color scale on the right-hand side represents the amplitude of the signal in volts. The received waveforms shown in Fig. 4 were taken at a position of 24 mm.

Fig. 7 contains the acoustic wavefront as a function of time and position for sample F12. The position axis was taken perpendicular to the fractures to examine the effect of the fractures on the propagating acoustic wavefront. For sample F12, pressure on the fractures strongly affects the propagating acoustic wavefront. For the condition at low pressure (Fig. 7a), strong energy confinement of the propagating wavefront is observed inside the central waveguide, with little energy outside the first set of fractures. In addition, the first arrival is delayed and strongly attenuated by the fractures, while the late-arriving energy is strong.

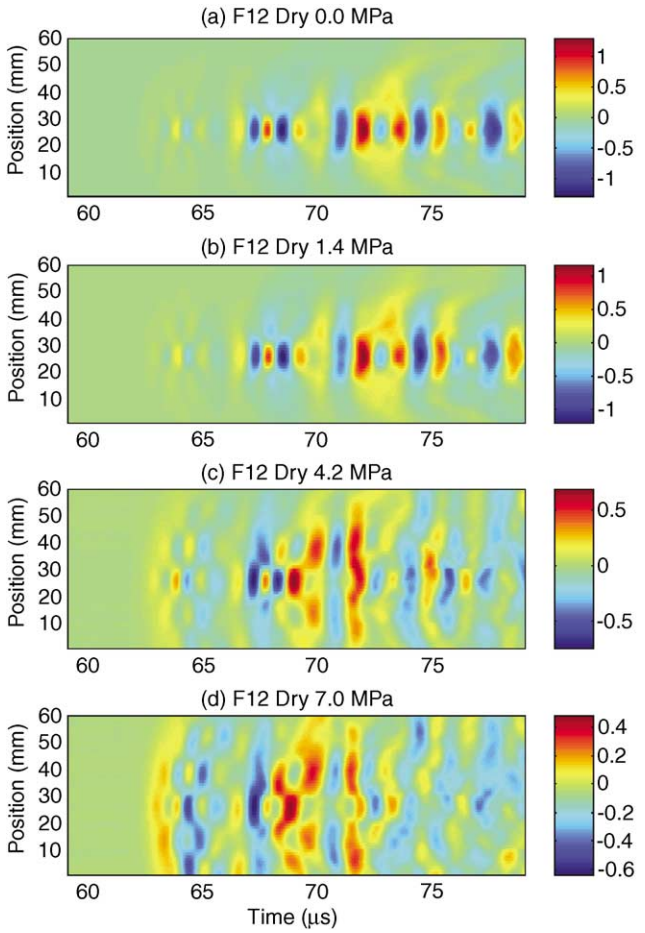

Fig. 7. The seismic wavefront as a function of position and time from sample F12 subjected to (a) 0 MPa, (b) 1.4 MPa, (c) 4.2 MPa, and (d) 7 MPa. The color scale on the right-hand side represents the amplitude of the signal in volts. The received waveforms shown in Fig. 5 were taken at a position of 24 mm. The five fractures probed in the sampling region are located at positions of 6, 18, 30, 42 and 54 mm.

As the pressure on the sample increases (Fig. 7d), the acoustic wavefront is observed to propagate across all five fractures in the data sampling region, which indicates that the specific stiffness of the fractures has increased under applied pressure. The arrival time of the compressional mode (the first arrival) wavefront is approximately equal to the arrival time of the compressional wave in the intact sample, although the wavefronts outside the central waveguide are delayed and attenuated by each fracture that the wavefront crosses. The image of the acoustic wavefront in Fig. 7b also indicates that the fracture specific stiffnesses for each fracture in sample F12 are not the same. The amplitude of the first arrival in the wavefront is more strongly attenuated by the fractures located at positions greater than 30 mm.

3.3. Wavefront images

Acoustic wavefront imaging was performed on the intact and fractured samples to observe the anisotropy produced by the multiple parallel fractures. The data from the wavefront imaging experiments represents the intersection of the spherical wavefront with the plane defining the receiving surface of the sample as a function of time. In this section, we examine the spatial distribution of acoustic energy that was measured for each sample.

Fig. 8 contains the wavefronts for sample FI, the intact sample, for an arrival time of 63.2 μs subjected to 0 and 7 MPa. The images represent a 60 mm × 60 mm region on the receiver side of the sample and the color represents the amplitude (red–high; blue–low). The

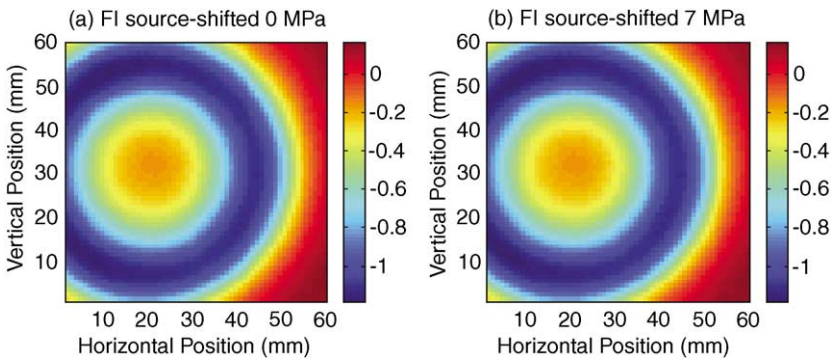

Fig. 8. The seismic wavefront as a function of space for an arrival time of 63.2 μs for the intact sample FI subjected to (a) 0 MPa and (b) 7 MPa. The color scale represents the amplitude of the signal in volts.

isotropy of sample FI is evident in the images (Fig. 8) by the circular shape of the wavefront, i.e., the wavefront spreads out with the same velocity and amplitude in all directions.

For sample F12, the spatial distribution of energy in the acoustic wavefront for an arrival time of 63.2 μs varied depending on the pressure. In Fig. 9, the fractures are oriented parallel to the vertical axis and are located at horizontal positions of approximately 6, 18, 30, 42 and 54 mm. At 0 MPa, the acoustic wavefront (Fig. 9a) is strongly confined by the two fractures that bracket the layer which contains the source (between horizontal position of 18 and 30 mm). The acoustic wavefront is delayed by the fractures and spreads out faster within the layer. The variation in fracture specific stiffness among the fractures is also evident from the wavefront. In Fig. 9a, the wavefront exhibits less attenuation and is delayed less when propagating across the fracture located at a horizontal position of 30 mm, than the portion of the wavefront that propagates across the fracture at 18 mm. When the pressure on sample F12 was increased to 1.4 MPa (Fig. 9b), the increased fracture specific stiffnesses result in higher transmission of energy across the fractures, smaller delay of the wavefront, and weaker energy confinement in the central layer between fractures. The trend continues with stresses at 4.2 and 7.0 MPa in Figs. 9c and d respectively. The non-uniform stiffness among the fractures in sample F12 is still evident at high pressure by the lack of symmetry in the wavefront.

3.4. Results from plane-wave transducers

3.4.1. Individual waveforms

Fig. 10 shows the transmitted waveforms for intact sample FI and sample F12 when the source and receiver were plane wave transducers that were co-axially aligned. Because applying a confining pressure to sample FI had no effect on the amplitude or arrival time of the waves, the waveforms of sample FI at 0 and 7 MPa are the same (shown at the top of the graph in Fig. 10). The waveform from the intact sample using the plane-wave transducer has a cleaner pulse compared to the waveform of the intact sample using the focused transducers (Fig. 4), i.e., most of the energy in the source is limited in a very narrow time window. The first arrival time for sample FI is ~ 0.60 μs later than that of sample F12, which is caused by the difference in sample lengths (sample FI is 4 mm longer than sample F12, giving the time delay due to the length difference as $\Delta L/V_p = (0.004\,\text{m})/(6500\,\text{m/s}) = 0.615\,\mu\text{s}$). For sample F12, the first arriving energy (~ 44 μs) exhibits a change in shape for increasing pressures while the second arriving energy group (~ 47 μs) exhibits a

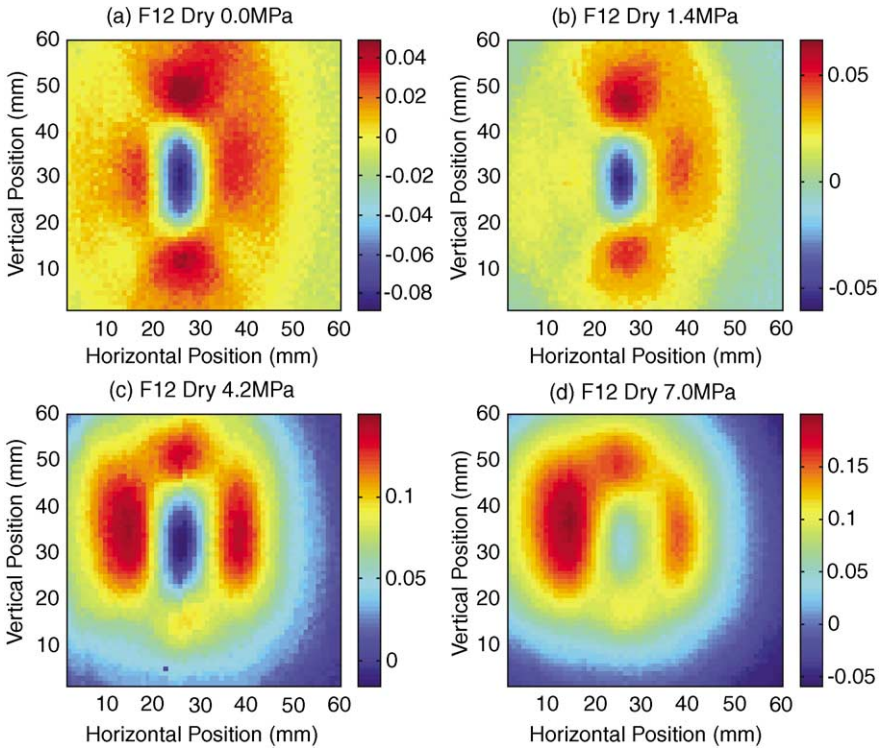

Fig. 9. The seismic wavefront as a function of space for an arrival time of 63.2 μs for sample F12 subjected to (a) 0 MPa, (b) 1.4 MPa, (c) 4.2 MPa, and (d) 7 MPa. The color scale represents the amplitude of the signal in volts. The five fractures probed in the sampling region are located at horizontal positions of 6, 18, 30, 42 and 54 mm.

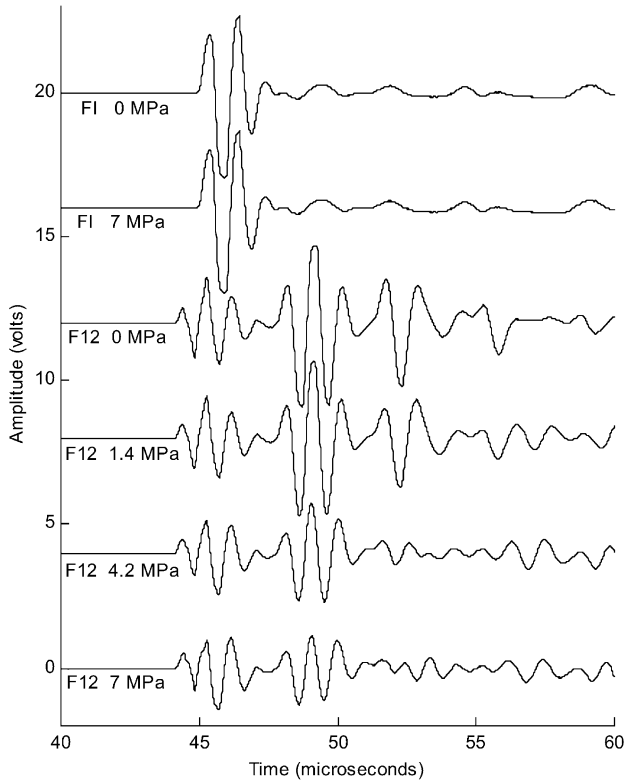

Fig. 10. The received waveforms from the intact sample FI subjected to 0 and 7 MPa, and from the fractured sample F12 subjected to 0, 1.4, 4.2 and 7 MPa when plane-wave source and receiver transducers are positioned across from each other.

decrease in amplitude with increasing pressures. The difference in arrival times between the waves obtained with the focused transducers and the waves obtained with the plane wave transducers is caused by the difference in the water path length between the transducers and the sample for the different set of transducers.

4. Analysis of plane-wave data

In our analysis of the data collected with the plane-wave transducers, we concentrate only on the compressional wave in the central layer that arrives around 44 μs (Fig. 10). We do not consider the modes that arrive at 47 μs and later because these are superpositions of reflected waves and confined plate waves. Because of the difficulty in decomposing the superposition, we will not discuss these later-arriving waves in this paper.

We identify the first arriving mode as the compressional (P) wave mode that is guided between the fractures. To support our identifications of the first wave arrival, we model the fractures with displacement discontinuity boundary conditions, and consider the self-consistency equations for P-waveguide modes.

4.1. Displacement discontinuity theory

The behavior of the fractures is represented by a non-welded contact with displacement discontinuity boundary conditions. Several investigators [7–11,17–23] have modeled a fracture as a non-welded contact which is assumed to have negligible thickness compared to the seismic wavelength. The non-welded contact is represented by a set of boundary conditions between two elastic halfspaces. The boundary conditions that describe the non-welded contact are: (1) The normal and shear stresses across the non-welded contact are assumed to be continuous ($\sigma_1 = \sigma_2$); and (2) the displacements are discontinuous by an amount inversely proportional to the specific stiffness of the fracture ($u_2 - u_1 = \sigma/\kappa$), where σ is stress, u is particle displacement, and κ is the specific stiffness of the fracture (Pa/m), and subscripts 1 and 2 refer to the elastic media on either side of the fracture. A fracture has both normal and shear components of specific stiffness. These boundary conditions for a non-welded contact have been referred to by several different names, such as slip interface model [7], the displacement discontinuity model [9], or the imperfect interface model [24]. This model reverts to the boundary conditions for a welded interface when $\kappa \to \infty$, and a free-surface when $\kappa \to 0$. The mechanical stiffness of a fracture depends on the spatial distribution and the amount of contact area within a fracture, and on the aperture distribution of the void space in a fracture [25–30].

The displacement discontinuity boundary conditions have been used to derive plane wave transmission and reflection coefficients [7–10,19], group time delays [31], interface waves [21,23], guided love waves [32], and P-Sv guided-waves [11,12]. For a single fracture, the displacement discontinuity theory predicts transmission and reflection coefficients, as well as a group time delay, that are found to be frequency dependent and to depend on the stiffness of the fracture, considered as a purely elastic model. In our analysis of wave-guiding of compressional waves between two fractures, we use the displacement discontinuity theory to calculate the phase shift upon reflection from a fracture to calculate the self-consistency condition for the existence of guided modes.

4.2. Waveguide self-consistency condition

Because a fracture behaves as a non-welded contact, wave-guiding between two parallel fractures results in a leaky wave-guide, i.e., for every reflection some portion of the energy will be transmitted across the fracture. The amount of energy loss from the wave-guide into the surrounding medium is a function of the frequency of

the signal and the specific stiffness of the fracture. Nonetheless, sufficient energy is reflected to allow waveguiding of a nonstationary guided mode that decays only weakly along the direction of propagation. We base our analysis of guiding of compressional waves between two fractures on a simple approach that includes the displacement discontinuity representation of fractures to calculate the phase shift for reflected compressional (P) waves.

We assume a monochromatic plane wave of wavelength, λ, wave number, k, and phase velocity, v. The wave is polarized in the direction of propagation (Fig. 11) and its wave vector lies in the y–z plane at an angle θ relative to the z-axis. The wave reflects from the upper fracture, travels at an angle of $-\theta$, and then reflects from the lower fracture and travels at an angle θ, and so on until it reaches the receiving face of the sample. A self-consistency condition is imposed that requires that after the wave reflects twice it exactly reproduces itself. Waves which satisfy this condition are called wave-guide modes which maintain the same transverse distribution and polarization at all distances along the wave-guide axis. This condition is mathematically expressed as

$$2\pi\overline{AC}/\lambda - 2\pi\overline{AB}/\lambda + 2\phi_{\mathrm{rp}} = 2\pi m \quad \text{where } m = 0, 1, 2, \ldots. \tag{1}$$

Because $\overline{AC} - \overline{AB} = 2d\sin\theta$,

$$4\pi d\sin\theta/\lambda + 2\phi_{\mathrm{rp}} = 2\pi m \quad \text{where} \quad m = 0, 1, 2, \ldots. \tag{2}$$

The self-consistency condition is therefore only satisfied for discrete angles of $\theta_m(\lambda)$ with mode number, m. The phase shift ϕ_{rp} is calculated from the compressional wave reflection coefficient, R_{p}, from the displacement discontinuity theory by

$$\phi_{\mathrm{rp}} = \tan^{-1}(imag(R_{\mathrm{p}})/real(R_{\mathrm{p}})). \tag{3}$$

A zero-solving program was used to find the angles between 0° and 90° for a given mode number, m, which satisfied Eq. (2). For the analysis, a range of fracture specific stiffnesses and signal frequencies where used.

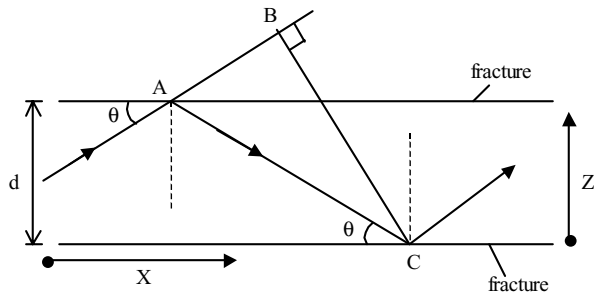

Fig. 11. Geometry used for waveguide analysis.

4.3. Waveguide modes and dispersion

The number of guided modes that satisfy the self-consistency Eq. (2) for sample F12 are shown in Fig. 12 as a function of frequency for selected stiffnesses between 1.0×10^{11} and 1.0×10^{15} Pa/m. Below a frequency of about 0.2 MHz, no guided modes exist for this range of stiffness, fracture spacing and sample length [34]. The first P-guided mode is supported for a frequency between 0.3 and 0.7 MHz, depending on the fracture stiffness. At the central frequency of 1.0 MHz of our experiment, only the three lowest-order guided P-wave modes satisfy the self-consistency criterion. The compressional-wave wavelength at 1.0 MHz is approximately 6.5 mm, compared with the width of the layer between the fractures of 12 mm. We therefore have the condition $d \approx 2\lambda$ for the P-mode waveguide in our experiment. For low frequencies and high stiffnesses, the P-wave experiences a $\pi/2$ phase shift shown in Fig. 13, compared to the phase shift of π for a seismic wave reflecting from a welded interface between media with unequal impedances. The shift in phase caused by modeling the fracture as a displacement discontinuity depends on the frequency of the signal and the fracture specific stiffness.

One of the most important features of guided waves is group velocity dispersion. This arises from two sources: one that is geometrical and the other that is dynamical. When solving the self-consistency equation, the parameter that determines self-consistency for a specific frequency is the bounce angle, θ_m, of the wave. Waves at higher frequency have shorter wavelength and must be

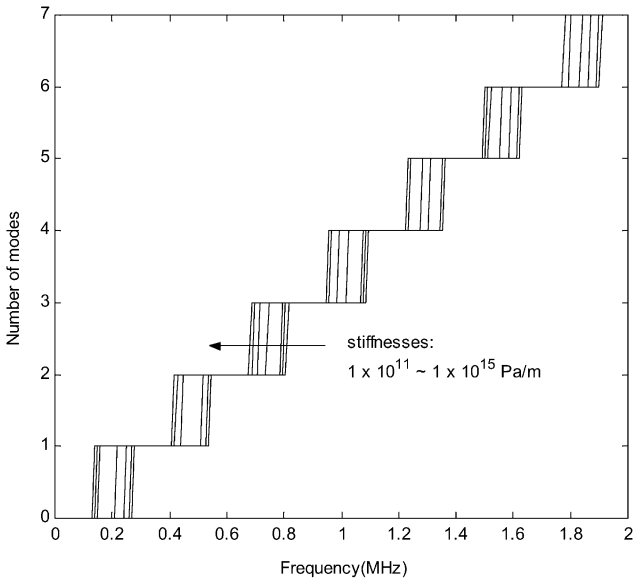

Fig. 12. The number of compressional-wave guided modes as a function of frequency for fracture specific stiffnesses ranging from 1.0×10^{11} to 1.0×10^{15} Pa/m.

incident on the fracture planes at shallower angles to satisfy self-consistency, which is shown in Fig. 14 for selected fracture stiffnesses for the $m = 0$ guided compressional-wave mode. Using a ray-approximation, the contribution of the bounce angle to the delay of the pulse arrival is

$$t_{\text{geom}} = L/(V_{\text{p}} \cos \theta_m) \tag{4}$$

At shallow angles obtained at high frequencies, the guided P-wave mode approaches the arrival time of the bulk *P*-wave.

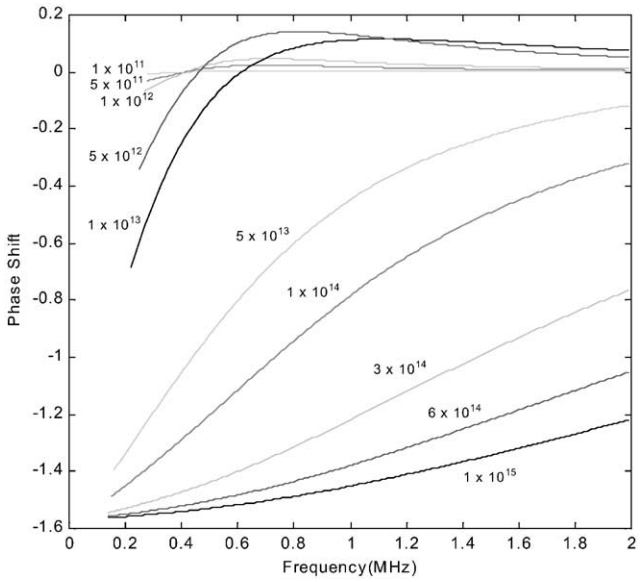

Fig. 13. Phase shift of the compressional wave upon reflection as a function of frequency for fracture specific stiffnesses ranging from 1.0×10^{11} to 1.0×10^{15} Pa/m.

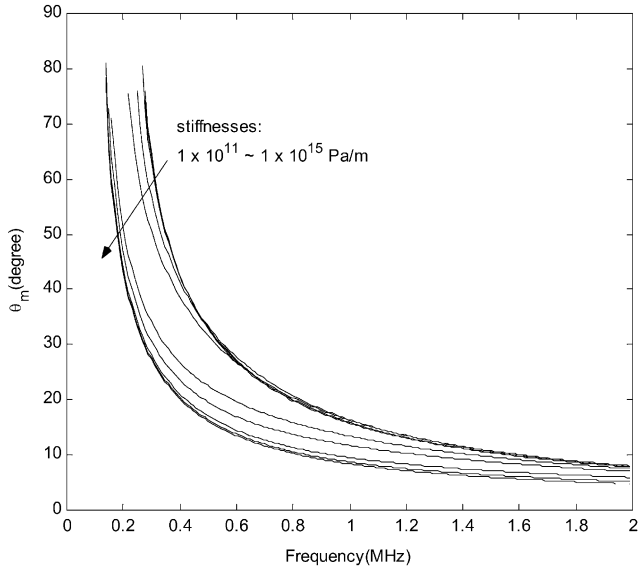

Fig. 14. θ_m for $m = 0$ as a function of frequency for fracture specific stiffnesses ranging from 1.0×10^{11} to 1.0×10^{15} Pa/m.

The second contribution to the guided mode group delay is the group delay that is experienced upon reflection at the fracture. The group delay per reflection is determined through the expression

$$t_{\text{g}} = \mathrm{d}\phi_{\text{rp}}/\mathrm{d}\omega \tag{5}$$

where ϕ_{rp} is the phase experienced upon reflection of the *P*-wave. The dynamical group delay experienced by the guided wave is

$$t_{\text{dynam}} = t_{\text{g}} N \tag{6}$$

where N is the number of bounces. The total group delay is

$$T_{\text{delay}} = t_{\text{geom}} + t_{\text{dynam}} \tag{7}$$

The contributions to the total group delay from the dynamical contribution compared with the total group delay are shown in Figs. 15(a) and (b). The dynamical

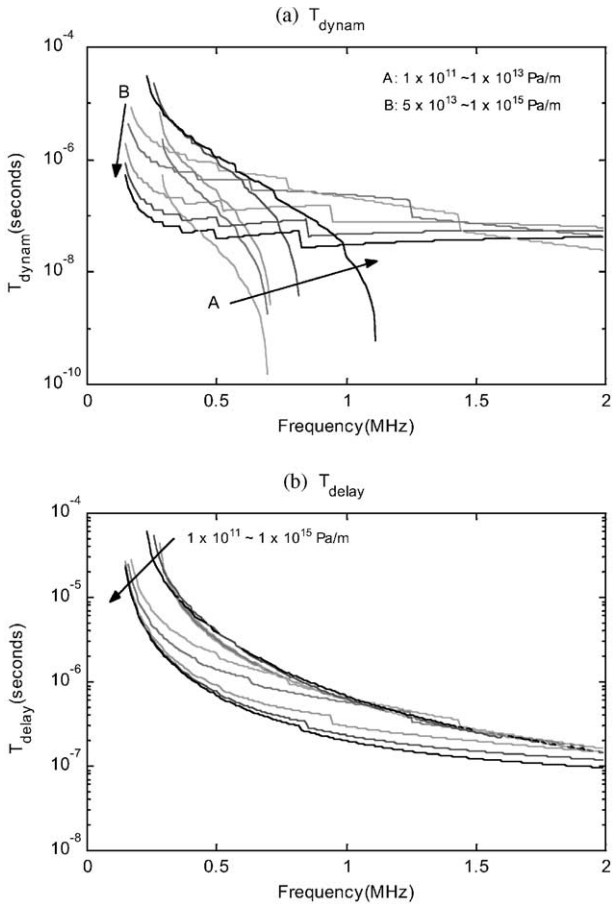

Fig. 15. (a) The accumulated dynamic group time delay from all of the reflections of a compressional wave as a function of frequency for fracture specific stiffnesses ranging from 1.0×10^{11} to 1.0×10^{15} Pa/m. The arrow labeled A indicates the curve generated by using fracture specific stiffnesses that ranged from 1×10^{11} to 1×10^{13} Pa/m. The arrow labeled B indicates the curve generated by using fracture specific stiffnesses that ranged from 5×10^{13} to 1×10^{15} Pa/m. (b) The total group time delay as a function of frequency for fracture specific stiffnesses ranging from 1.0×10^{11} to 1.0×10^{15} Pa/m.

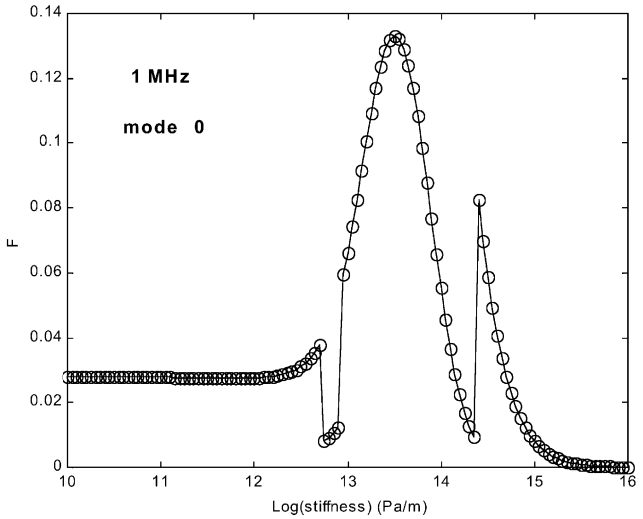

Fig. 16. The energy remaining (Eq. (8)) in the guided compressional-wave mode as a function of fracture specific stiffness for a frequency of 1.0 MHz for $m = 0$.

contribution at 1.0 MHz (for a fracture specific stiffness of 1.0×10^{14} Pa/m) is $\sim 0.24\,\mu s$ compared to the geometric contribution of $\sim 0.33\,\mu s$. Thus the compressional guided-mode is delayed relative to the direct compressional mode by $\sim 0.57\,\mu s$.

The final theoretical aspect of a leaky guided mode that we need to consider before analyzing the experimental data in the context of the theoretical results is the amplitude of the evanescent guided wave. The *P*-guided-wave sheds energy into two modes as it propagates: converted *S*-waves that propagate inside the guide layer, and transmitted modes that propagate in the outer layers. An estimate of the energy remaining in the guided *P*-wave can be made based on the bounce angle θ_m and the *P–P* reflection coefficient that depends on θ_m. The fraction of remaining *P*-mode energy is given by

$$F = \left| \boldsymbol{R}_{\mathrm{p}}^{2} \right|^{N}, \tag{8}$$

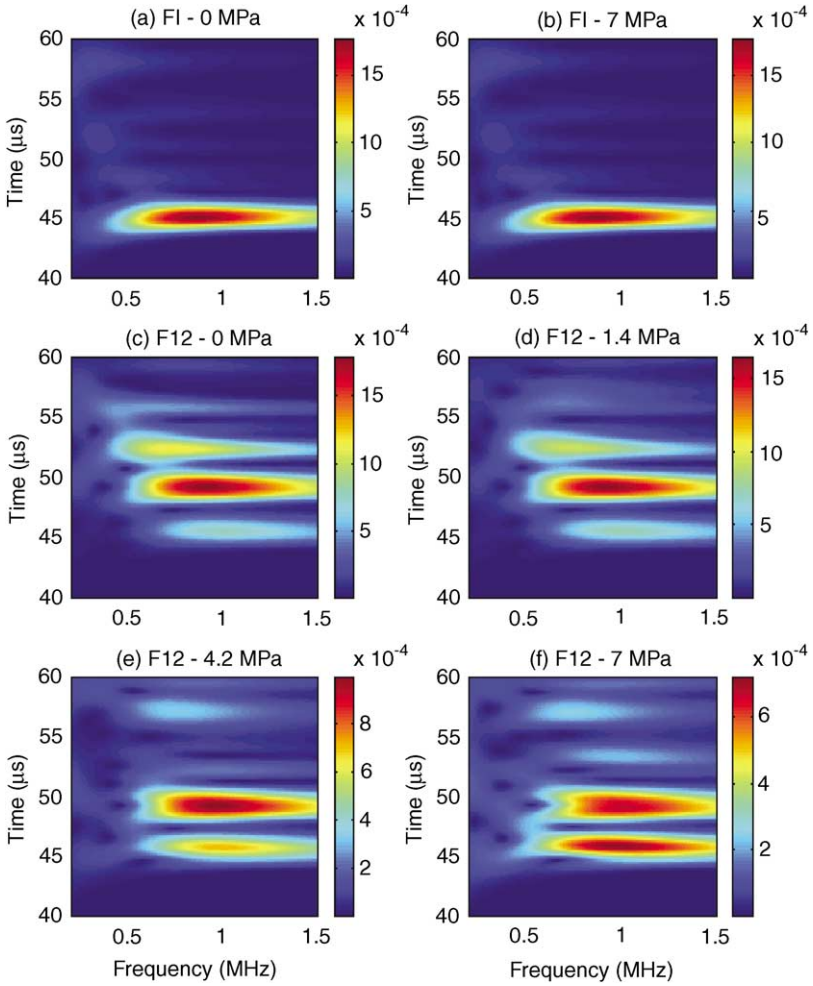

Fig. 17. The wavelet transforms of the received waveforms shown in Fig. 10 for sample FI and sample F12. Wavelet transformation for (a) FI under 0 MPa, (b) FI under 7 MPa, (c) F12 under 0 MPa, (d) F12 under 1.4 MPa, (e) F12 under 4.2 MPa, and (f) F12 under 7 MPa. Color represents the strength of the transform with red representing high values and purple representing low values. The amplitude for each wavelet transform is given by the color bar to the right of the wavelet transformation.

where N is the number of bounces. The fraction of remaining compressional guided-mode energy is graphed in Fig. 16 as a function of stiffness for a frequency of 1.0 MHz. The remaining energy is not a monotonic function in stiffness because the mode angle depends on the frequency and on fracture specific stiffness.

4.4. Wavelet frequency analysis

To analyze the frequency dispersion in the experimental data, a wavelet analysis was used to determine the time-frequency relationship. For this analysis, a Hilbert wavelet method [33] was used that provides equal accuracy in time and frequency. The wavelet group transforms are shown in Fig. 17 for the intact sample, FI, and for sample F12 at 0, 1.4, 4.2 and 7 MPa.

The transducers used in this experiment have a positive chirp (Fig. 17) in which higher frequencies arrive later, as observed in the data for the intact sample. The chirp is unaffected by pressure for the intact sample. The compressional-guided mode can be seen in the F12 wavelet transforms ($\sim$45 μs). The time dispersion is now negative, with higher frequencies arriving earlier (Fig. 17). A negative time dispersion is consistent with the behavior of a guided mode (Fig. 15b). The waveguide dispersion of the P-mode has therefore more than compensated the original positive chirp of the transducers.

A quantitative study of the group delay is performed by tracing the gradient of the group wavelet transforms of Fig. 17. The results as a function of frequency are shown in Fig. 18 for F12 after subtraction of the system chirp. The time-dispersion for the guided compressional-mode obtained from the wavelet transforms in Fig. 17 as a function of frequency for sample F12 for (a) 0 MPa, (b) 1.4 MPa, (c) 4.2 MPa, and (d) 7 MPa are shown in Fig. 18. The total time delay, as calculated from the theory, is given by the dashed and solid line curves. The lower left dashed curve represents the predicted total time delay as a function of frequency for a fracture specific stiffness of $1 \times 10^{14.5}$ Pa/m. The upper right dashed curve represents the predicted total time delay as a function of frequency for a fracture specific stiffness of $1 \times 10^{14.15}$ Pa/m. The solid curve represents the best-fit predicted total time delay as a function of frequency for a fracture specific stiffness of $1 \times 10^{14.3}$ Pa/m. The time dispersion of the guided compressional-wave is negative which is consistent with the theory for compressional-mode wave guiding.

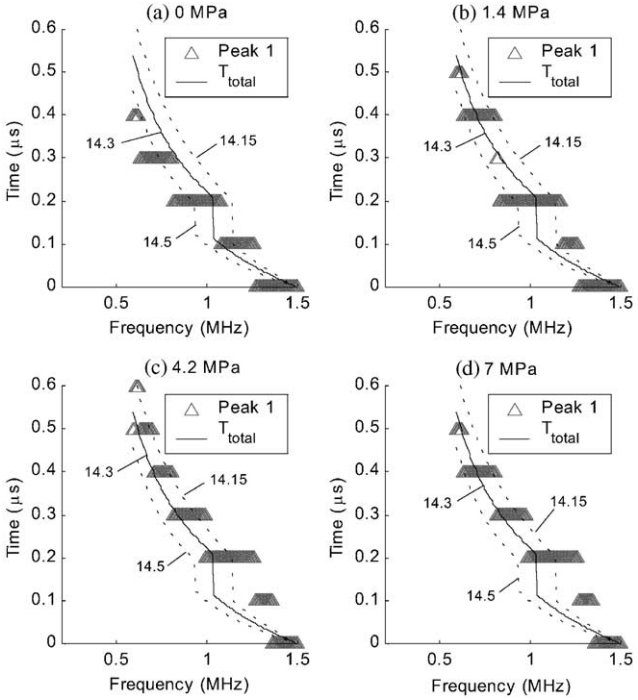

Fig. 18. The time-dispersion for the guided compressional-mode obtained from the wavelet transforms in Fig. 17 as a function of frequency for sample F12 for (a) 0 MPa, (b) 1.4 MPa, (c) 4.2 MPa, and (d) 7 MPa. Total time delay, as calculated from the theory, is given by the dashed and solid line curves. The lower left dashed curve represents the predicted total time delay as a function of frequency for a fracture specific stiffness of $1 \times 10^{14.5}$ Pa/m. The upper right dashed curve represents the predicted total time delay as a function of frequency for a fracture specific stiffness of $1 \times 10^{14.15}$ Pa/m. The solid curve represents the best-fit predicted total time delay as a function of frequency for a fracture specific stiffness of $1 \times 10^{14.3}$ Pa/m.

5. Conclusions

Images of the propagating wavefront in a medium containing multiple parallel fractures clearly shows that seismic energy is confined between fractures in an otherwise homogeneous and isotropic medium. The only anisotropy in the samples was produced by the presence of parallel fractures. The amount of energy confined between parallel fractures was observed to be a function of pressure. As pressure was increased on the sample, the fracture specific stiffness increased and more energy leaked out of the waveguide formed by the parallel fractures. Application of a wave-guiding theory for a waveguide formed by two parallel fractures, showed that a guided compressional wave can exist and the existence of this "leaky" guided mode is a function of fracture specific stiffness, fracture spacing and signal frequency. The "leaky" compressional-mode guided wave exhibits a negative time dispersion, i.e., high frequencies arrive first.

The results presented in this laboratory study using MHz frequencies can be translated to field-scale frequencies of kHz because two frequency scales are present simultaneously in the parallel-fracture sample. First, the fracture response to seismic waves has an intrinsic frequency set by the ratio of the fracture stiffness divided by the seismic impedance of the

medium. Fractures in rock with stiffnesses of 1×10^{10} Pa/m have characteristic frequencies of 1 kHz that are compatible with field-scale sources. Similarly, the spacing between the fractures sets a frequency scale. For a seismic wave with a frequency of 1 kHz, a fracture spacing of $d = 6$ m corresponds to the physical situation $d \approx 2\lambda$ studied in this paper. Also, we observed the evanescent guided modes at an observation distance of $L = 15\lambda$, which would correspond to an observation distance of 90 m in the field using 1 kHz sources. This distance is compatible with cross-hole seismic tomography.

Finally, by understanding the energy conversion from bulk waves to guided-modes, information about the mechanical properties of a fracture, namely fracture specific stiffness, can be predicted from laboratory as well as field data. By examining the change in energy among different guided-modes, it may be possible to monitor changes in fracture specific stiffness caused by stress, fluid-saturation or chemical alteration.

Acknowledgements

The authors wish to acknowledge Seiji Nakagawa for his thorough review of the paper and his useful comments. The authors also acknowledge support of this research by the Geosciences Research Program, Office of Basic Energy Sciences, and US Department of Energy; and equipment support from the National Science Foundation (9521686-CMS). LJPN wishes to acknowledge the National Science Foundation—Young Investigator Award (EAR-9896057 & EAR-9458373).

References

[1] Nur A. Effects of stress on velocity anisotropy in rocks with cracks. J Geophys Res 1971;76(8):2022–34.
[2] Hudson JA. Wave speeds and attenuation of elastic waves in material containing cracks. Geophys J Roy Astro Soc 1981;64:133–50.
[3] Crampin S. Effective anisotropic elastic constants for wave propagation through cracked solids. Geophys J Roy Astron Soc 1984;76:133–45.
[4] Schoenberg M, Muir F. A calculus for finely layered anisotropic media. Geophysics 1989;54:581–9.
[5] Hood JA, Schoenberg M. Estimation of vertical fracturing from measured elastic moduli. J Geophys Res 1989;94:15611–8.
[6] Schoenberg M, Sayers CM. Seismic anisotropy of fractured rock. Geophysics 1995;60:204–11.
[7] Schoenberg M. Elastic wave behavior across linear slip interfaces. J Acoust Soc Am 1980;5(68):1516–21.
[8] Kitsunezaki C. Behavior of plane waves across a plane crack. J Min Coll Akita Univ Ser A 1983;3(6):173–87.
[9] Pyrak-Nolte LJ, Myer LR, Cook NGW. Transmission of seismic waves across single natural fractures. J Geophys Res B 1990;6(95):8617–38.
[10] Pyrak-Nolte LJ, Myer LR, Cook NGW. Anisotropy in seismic velocities and amplitudes from multiple parallel fractures. J Geophys Res B 1990;7(95):11345–58.
[11] Nakagawa S. Acoustic resonance characteristics of rock and concrete containing fractures. Ph.D. Thesis, University of California, Berkeley, 1998.
[12] Nihei KT, Yi W, Myer LR, Cook NGW, Schoenberg M. Fracture channel waves. J Geophys Res 1999;104(B3):4769–81.
[13] Nagy PB, Bonner BP, Adler L. Slow wave imaging of permeable rocks. Geophys Res Lett 1995;22(9):1053–6.
[14] Mullenbach BL, Acoustic imaging of sediments. Master Thesis. University of Notre Dame, NotreDame, IN, USA, 1996.
[15] Pyrak-Nolte LJ, Mullenbach BL, Roy S. Interface waves along fractures. J Appl Geophys 1996;35:79–87.
[16] Hauser MR, Weaver RL, Wolfe JP. Internal diffraction of ultrasound in crystals: phonon focusing at long wavelengths. Phys Rev Lett 1992;68:2605–7.
[17] Mindlin RD. Waves and vibrations in isotropic planes. In: Goodier JW, Hoff WJ, editors. Structural Mechanics. Oxford: Pergammon, 1960. p. 199.
[18] Kendall K, Tabor D. An ultrasonic study of the area of contact between stationary and sliding surfaces. Proc Roy Soc London A 1971;323:321–40.
[19] Schoenberg M. Reflection of elastic waves from periodically stratified media with interfacial slip. Geophys Pros 1983;31:265–92.
[20] Myer LR, Hopkins D, Cook NGW. Effects of contact area of an interface on acoustic wave transmission characteristics. Proceedings of 26th US Rock Mechanics Symposium. Rotterdam: A.A. Balkema, 1985. p. 565–72.
[21] Pyrak-Nolte LJ, Cook NGW. Elastic interface waves along a fracture. Geophys Res Let 1987;11(14):1107–10.
[22] Suarez-Rivera R. The influence of thin clay layers containing liquids on the propagation of shear waves. Ph.D. Thesis, University of California, Berkeley, 1992.
[23] Gu B. Interface waves on a fracture in rock. Ph.D. Thesis, University of California, Berkeley, 1994.
[24] Rokhlin SI, Wang YJ. Analysis of boundary conditions for elastic wave interaction with an interface between two solids I. Acoustic Soc Am 1991;65(8):503–15.
[25] Greenwood JA, Williamson JBP. Contact of nominally flat surfaces. Proc Roy Soc London A 1966;300–19.
[26] Gangi AF. Variation of whole- and fractured-porous-rock permeability with confining pressure. Int J Rock Mech Min Sci Geomech Abstr 1978;15:249–57.
[27] Brown SR, Scholz CH. Closure of random surfaces in contact. J Geophys Res 1985;90:5531.
[28] Brown SR, Scholz CH. Closure of rock joints. J Geophys Res 1986;91:4939.
[29] Hopkins DL, Cook, NGW, Myer LR. Fracture stiffness and aperture as a function of applied stress and contact geometry. Rock Mechanics: Proceedings of the 28th US Symposium. 1987. p. 673–80.
[30] Hopkins DL, Cook NGW, Myer LR. Normal joint stiffness as a function of spatial geometry and surface roughness. International Symposium on Rock Joints 1990. p. 203–10.
[31] Pyrak-Nolte LJ. Seismic visibility of fractures. Ph.D. Thesis, University of California, Berkeley, 1988.
[32] Nihei KT, Myer LR, Cook NGW, Yi W. Effects of non-welded interfaces on guided SH–waves. Geophys Res Lett 1994; 21(9):745–8.
[33] Nolte DD, Pyrak-Nolte LJ, Ziegler C, Beachy J. Transition from the displacement discontinuity limit to the resonant scattering regime for fracture interface waves. Int J Rock Mech Min Sci Geomech Abstr 2000;37:245–62.
[34] Xian C. Wavefront imaging of energy confinement by multiple parallel fractures. M.S. Thesis, Purdue University, West Lafayette, Indiana, 2001.